nature physics

LETTERS

PUBLISHED ONLINE: 31 AUGUST 2014 | DOI: 10.1038/NPHYS3075

Gate-dependent pseudospin mixing in graphene/boron nitride moiré superlattices

Zhiwen Shi[1†], Chenhao Jin[1†], Wei Yang[2], Long Ju[1], Jason Horng[1], Xiaobo Lu[2], Hans A. Bechtel[3], Michael C. Martin[3], Deyi Fu[4], Junqiao Wu[4,5], Kenji Watanabe[6], Takashi Taniguchi[6], Yuanbo Zhang[7], Xuedong Bai[2], Enge Wang[8], Guangyu Zhang[2]* and Feng Wang[1,5,9]*

Electrons in graphene are described by relativistic Dirac–Weyl spinors with a two-component pseudospin[1–12]. The unique pseudospin structure of Dirac electrons leads to emerging phenomena such as the massless Dirac cone[2], anomalous quantum Hall effect[2,3], and Klein tunnelling[4,5] in graphene. The capability to manipulate electron pseudospin is highly desirable for novel graphene electronics, and it requires precise control to differentiate the two graphene sublattices at the atomic level. Graphene/boron nitride moiré superlattices, where a fast sublattice oscillation due to boron and nitrogen atoms is superimposed on the slow moiré period, provides an attractive approach to engineer the electron pseudospin in graphene[13–18]. This unusual moiré superlattice leads to a spinor potential with unusual hybridization of electron pseudospins, which can be probed directly through infrared spectroscopy because optical transitions are very sensitive to excited state wavefunctions. Here, we perform micro-infrared spectroscopy on a graphene/boron nitride heterostructure and demonstrate that the moiré superlattice potential is dominated by a pseudospin-mixing component analogous to a spatially varying pseudomagnetic field. In addition, we show that the spinor potential depends sensitively on the gate-induced carrier concentration in graphene, indicating a strong renormalization of the spinor potential from electron–electron interactions.

Electron pseudospin in graphene describes the contribution of two sublattices to the electron wavefunction, which leads to many fascinating transport and optical properties[1–12]. The control of pseudospin, such as opening a pseudospin gap at the Dirac point[19–25], is highly desirable for graphene's application in electronics and photonics. Graphene on atomically flat hexagonal boron nitride (BN) is a promising candidate for pseudospin engineering owing to its remarkably high electron mobility[26] and the unique graphene/BN interactions[13–18]. It has been demonstrated recently that new mini-Dirac points and Hofstadter butterfly patterns can emerge from the moiré superlattice in graphene/BN heterostructures[14–18]. A particularly intriguing property of the moiré superlattice is that the fast oscillation at B and N sublattice sites leads to a periodic spinor potential in graphene that is described by a two-by-two tensor rather than a scalar[27,28]. This spinor potential couples efficiently to the electron pseudospins, and it was invoked to explain the finite bandgap at the Dirac point in graphene/BN heterostructures[17,28,29]. However, direct observation of the spinor potential has been challenging. For example, the density of states change in graphene/BN heterostructures revealed by previous scanning tunnelling spectroscopy (STS) and transport measurements can be largely accounted for by a scalar periodic potential[13–18].

Here, we use infrared spectroscopy to probe the spinor potential in the moiré superlattice. It has been recently predicted that the optical conductivity of graphene can exhibit distinctively different behaviour in a spinor potential from that in a scalar potential[30]. We demonstrate experimentally that the pseudospin-mixing potential indeed plays a dominant role in optical absorption spectra of graphene/BN heterostructures, owing to the sensitive dependence of the optical transition matrix on the hybridized electron wavefunctions. We show that the pseudospin-mixing potential, unlike a scalar potential, can hybridize electron waves with opposite pseudospins and open an 'inverse gap' at the boundary of the superlattice Brillouin zone. In addition, we show that the spinor potential depends sensitively on the carrier concentration in graphene, indicating a strong renormalization of the spinor potential from electron–electron interactions.

Our graphene samples were directly grown on hexagonal BN substrates following a van der Waals epitaxy mode[18]. Figure 1a shows an atomic force microscopy (AFM) image of a typical graphene/BN heterostructure, revealing a high coverage of monolayer graphene together with a small portion of bilayer graphene (bright area ∼0.3%) and bare BN (dark area ∼3%). In the high-resolution AFM image (Fig. 1a(inset)), a triangular moiré superlattice is clearly observed. The moiré period of 15 ± 1 nm matches well with the lattice constant difference between graphene (2.46 Å) and BN (2.50 Å), suggesting that the epitaxial graphene has a zero lattice twisting angle with BN (ref. 18). Two-terminal field-effect graphene devices with back-gate geometry (Figs 1b and 2a) were fabricated for electrical and optical characterizations. Figure 1c shows the room-temperature transport properties of a typical graphene/BN sample, which exhibits two prominent resistance peaks. The behaviour is similar to that observed in previous studies[15–18], where the resistance

[1]Department of Physics, University of California at Berkeley, Berkeley, California 94720, USA, [2]Beijing National Laboratory for Condensed Matter Physics and Institute of Physics, Chinese Academy of Sciences, Beijing 100190, China, [3]Advanced Light Source Division, Lawrence Berkeley National Laboratory, Berkeley, California 94720, USA, [4]Department of Materials Science and Engineering, University of California at Berkeley, Berkeley, California 94720, USA, [5]Materials Science Division, Lawrence Berkeley National Laboratory, Berkeley, California 94720, USA, [6]Advanced Materials Laboratory, National Institute for Materials Science, 1-1 Namiki, Tsukuba 305-0044, Japan, [7]State Key Laboratory of Surface Physics and Department of Physics, Fudan University, Shanghai 200433, China, [8]International Centre for Quantum Materials, Peking University, Beijing 100871, China, [9]Kavli Energy NanoSciences Institute at the University of California, Berkeley and the Lawrence Berkeley National Laboratory, Berkeley, California, 94720, USA. †These authors contributed equally to this work. *e-mail: gyzhang@aphy.iphy.ac.cn; fengwang76@berkeley.edu

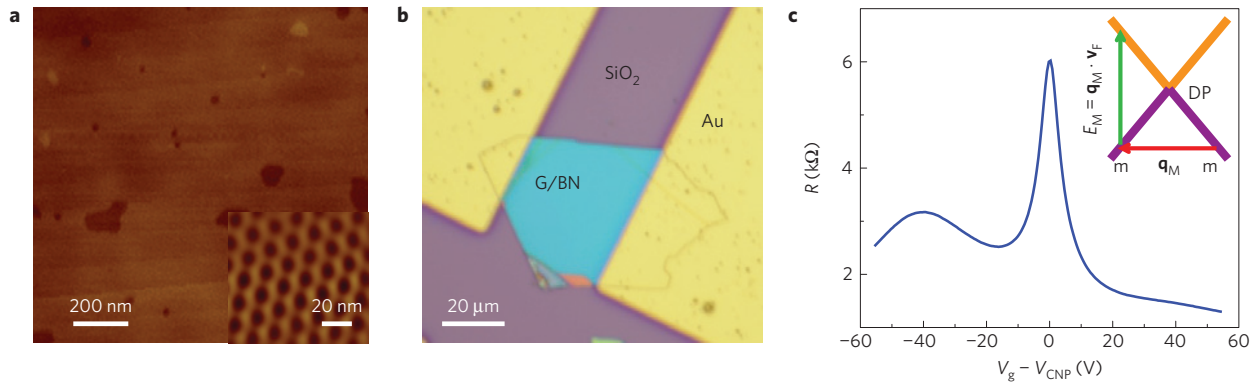

Figure 1 | Graphene/BN heterostructure and typical transport property. a, Atomic force microscopy image showing a high coverage of monolayer graphene together with a small portion of bilayer graphene (bright area ~0.3%) and bare BN (dark area ~3%). The inset shows a high-resolution AFM image of the graphene/BN moiré superlattice with a period of 15 ± 1 nm. **b**, Optical micrograph of a two-terminal field-effect graphene/BN device on a SiO_2/Si substrate. **c**, Gate-dependent resistance of a typical graphene/BN device at room temperature. The resistance peaks at $V_g = 0$ V and $V_g = -40$ V, corresponding to the original Dirac point (DP) and the mini-Dirac points on the hole side at the m point of the superlattice Brillouin zone, respectively. The inset shows the linear band of graphene. The moiré wavevector $\mathbf{q}_M$ (red arrow) connects the superlattice m point. Optical transitions at the m point have energy $E_M = \mathbf{q}_M \cdot \mathbf{v}_F$ (green arrow).

peaks at $V_g = 0$ V and $V_g = -40$ V were attributed respectively to the original Dirac point and the mini-Dirac points on the hole side at the m point of the superlattice Brillouin zone (see Figs 1c(inset) and 3a). The resistance peak on the hole side suggests a strong coupling between the zero-twisting graphene and BN layers, and a significant electron–hole asymmetry compared to the much weaker feature on the electron side.

To probe the pseudospin mixing potential from the moiré superlattice, we performed infrared micro-spectroscopy on graphene/BN heterostructures (Fig. 2a). Figure 2b shows a two-dimensional plot of the transmission spectra difference $T - T_{CNP}$ at different gate voltages V_g (or equivalently, Fermi energies E_F), where T_{CNP} is the transmission spectrum at the charge neutral point (CNP). The Fermi energy is extracted by $E_F = 26.3 \cdot V_g^{1/2}$ (meV) for this sample (Supplementary Section 1). The infrared spectra are largely symmetric for electron and hole doping, and show two distinct features: a relatively broad increase of light transmission that systematically shifts to higher energies with increasing E_F; and a sharp resonance-like feature at approximately 380 meV (black dashed line). The broad feature is due to Pauli blocking of interband transitions in bare graphene, which is similar to that observed in graphene on SiO_2/Si substrates[7–9]. The sharp feature shows decreased absorption at 380 meV in gated graphene, and is present only in the graphene/BN heterostructure. This energy matches well with the moiré energy $E_M \equiv \hbar \mathbf{v}_F \cdot \mathbf{q}_M$ (green arrow in Fig. 1c(inset)), where $\mathbf{q}_M$ is the wavevector of the moiré pattern and $\mathbf{v}_F$ is the graphene Fermi velocity[14]. Therefore, this sharp feature clearly originates from the graphene/BN moiré superlattice. Figure 2c shows detailed transmission spectra $T - T_{CNP}$ at several representative electron doping levels that are extracted from horizontal line cuts of Fig. 2b. To better examine the sharp feature associated with the moiré superlattice, we subtract the relative broad background and obtain, in Fig. 2d, the moiré-superlattice-induced optical conductivity change, labelled as σ^M, around the moiré energy E_M (Supplementary Section 2). Here we have made use of $\sigma^M_{70V} = 0$, because with $V_g = 70$ V ($E_F = 220$ meV) the mini-band optical absorption around E_M is negligible owing to Pauli blocking at $2E_F > E_M$. Figure 2d shows a significant absorption peak (corresponding to an increase in optical conductivity) at the moiré energy E_M for charge neutral graphene. This absorption peak at E_M is opposite to the change in the electron density of states, which shows a prominent dip at $E_M/2$ as observed in previous transport and STS measurements[14–18]. This 'inverse' behaviour indicates a critical role of the optical transition matrix resulting from the unusual electron wavefunction hybridization in graphene on BN. Figure 2d also shows that even slight electron doping can markedly modify the absorption peak at E_M.

To understand the infrared spectra in graphene/BN heterostructures, we need to investigate in detail how the spinor potential from the moiré superlattice modifies the optical absorption in graphene. A general form of the spinor potential can be written as $V = \sum_{j=1}^{6} V_j e^{i\mathbf{q}_j \cdot \mathbf{r}}$, where $\mathbf{q}_j$ are the reciprocal lattice vectors of the moiré superlattice with $|\mathbf{q}_j| = q_M$ (refs 27,28). As q_M is much smaller than the valley separation of graphene's original Brillouin zone, the two valleys are effectively decoupled. We can therefore focus on one valley, and determine the other valley by time-reversal symmetry. With the three-fold rotational symmetry and Hermitian requirement, only one among the six V_j is independent, and it can be parameterized with three real numbers u_0, u_3, u_1 as[27,28].

$$V_1 = V_0 \begin{pmatrix} u_0 + iu_3 & u_1 \\ u_1 & u_0 - iu_3 \end{pmatrix}$$

Here, V_0 is a constant characterizing the coupling strength between graphene and the BN substrate. The resulting electron eigenwavefuction and eigenenergy can be obtained through direct diagnolization of the Hamiltonian $H = \hbar \mathbf{v}_F \boldsymbol{\sigma} \cdot \mathbf{p} + V$ in the superlattice Brillouin zone. The original Dirac point is at the centre γ of the superlattice Brillouin zone, and the high-symmetry points at the zone boundary are labelled as m and k/k′, respectively (Fig. 3a).

The three parameters (u_0, u_3, u_1) represent three different types of potential with distinct physical meanings. The u_0 term describes a simple scalar potential symmetric at the two sublattices, that is, a pseudospin-blind potential. The u_3 term characterizes the local asymmetry of A–B sublattices, and can be considered as a pseudospin-dependent potential. The off diagonal term u_1 mixes the A–B sublattices similar to a pseudo-magnetic field, and can be considered as a pseudospin-mixing potential. These three different types of potential have completely different effects on electron pseudospin, wavefunction hybridization and optical transitions.

Figure 3b–d shows the optical conductivity changes due to pure u_0, u_3 and u_1 potentials with $V_0 = 10$ meV, respectively. The insets show the corresponding electronic band dispersion along the γ–m direction (red line in Fig. 3a) in each case. The optical

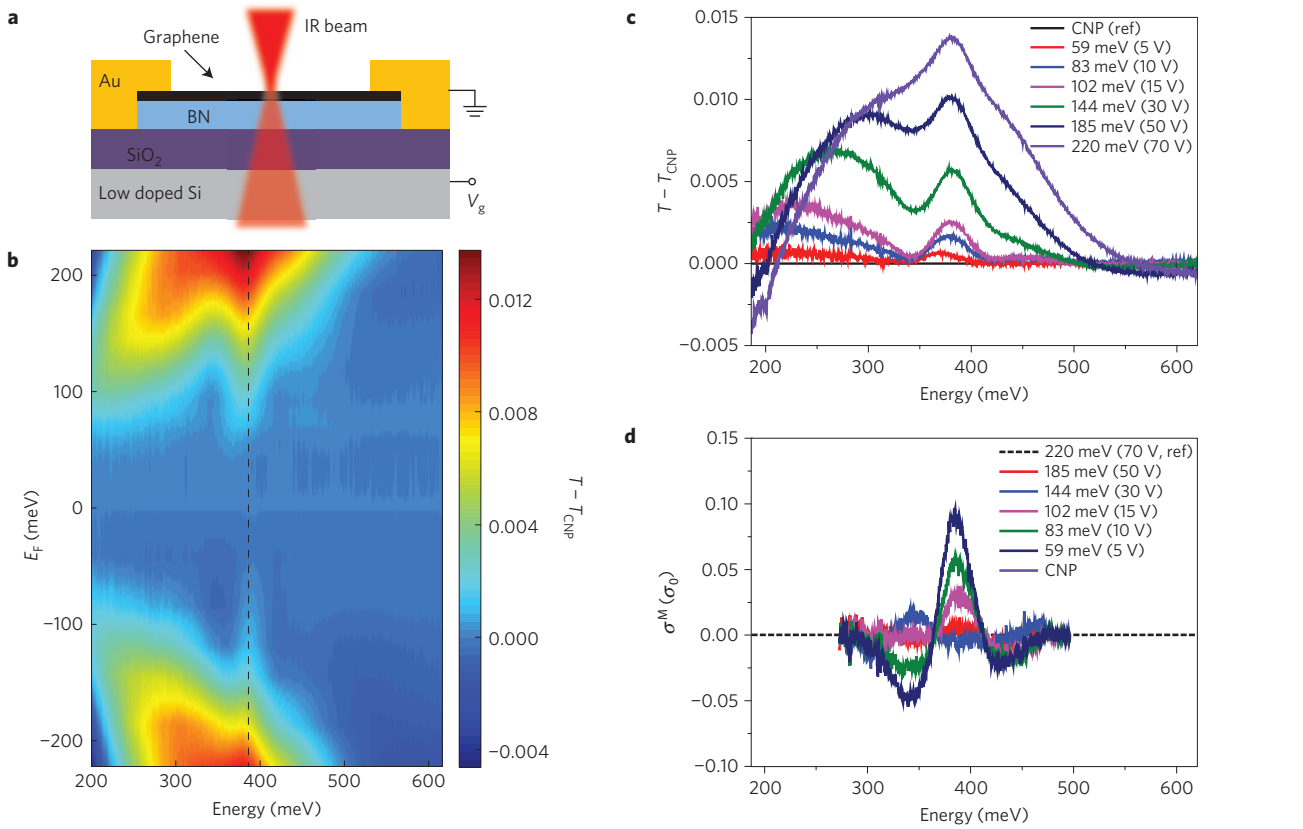

Figure 2 | Infrared micro-spectroscopy of the graphene/BN heterostructure. a, Schematic drawing of the experimental set-up. **b**, Two-dimensional plot of the transmission spectra difference $T - T_{CNP}$ at different Fermi energies E_F, where T_{CNP} is the transmission spectrum for graphene at the charge neutral point (CNP). The sharp feature at approximately 380 meV (black dashed line) originates from the moiré superlattice. The broad feature that shifts with E_F is due to Pauli blocking of interband transitions. **c**, Transmission spectra at $T - T_{CNP}$ for several representative electron doping levels (Fermi energies and corresponding gate voltages are shown in the legend), extracted from horizontal line cuts of **b**. **d**, Moiré-superlattice-induced optical conductivity change σ^M at different gate voltages. $\sigma_0 = \pi e^2/2h$ is the universal conductivity of graphene.

conductivity change can be best understood by considering electronic states around the m point in the superlattice Brillouin zone (Supplementary Sections 3 and 4). The pseudospin-blind potential u_0 cannot backscatter Dirac electrons in graphene[4,5]. Therefore, no gap is opened at the m point and a new mini-Dirac point emerges (Fig. 3b(inset)). With zero gap at the m point, the effect of a pseudospin-blind potential on the optical absorption is rather small (Fig. 3b). The pseudospin-dependent potential u_3 and pseudospin-mixing potential u_1, on the other hand, can couple electronic states with opposite pseudospins and both open a nontrivial gap at the m point. However, the hybridized electron wavefunctions at the gapped m point are distinctly different for the u_3 and u_1 terms, which can be probed directly through optical transitions. For the pseudospin-dependent potential u_3, only transitions from 1e to 1h and from 2e to 2h sub-band are allowed close to the mini-gap (Fig. 3c(inset) and Supplementary Section 4). In this case, the absorption spectrum mimics the electron density of states[13,14], except that the energy scale is multiplied by two, and it shows an absorption dip at 380 meV (Fig. 3c). The mini-gap generated by u_3 can therefore be termed as a 'normal' gap. The pseudospin-mixing potential u_1, on the other hand, restricts the optical transitions to the largely parallel 1e–2h and 2e–1h sub-bands (Fig. 3d (inset) and Supplementary Section 4). Transitions between the parallel bands lead to a van Hove singularity in the joint density of states and to a large absorption peak at E_M (Fig. 3d), opposite to the case in Fig. 3c. We term the mini-gap generated by u_1 as an 'inverse' gap. Our simulated optical conductivity is also consistent with results in ref. 30.

When u_0, u_1 and u_3 are all finite, their interplay further modifies the electron hybridization and optical spectra. The size of the mini-gap at the m point is described by $u_3 \pm u_1$ for the valence/conduction band. The relative magnitude of $|u_1|$ and $|u_3|$ strongly affects the nature of the mini-gap, which crosses zero for either the valence or conduction band at $|u_1| = |u_3|$. When $|u_1| < |u_3|$, the mini-gap is more similar to a 'normal' gap induced by a pure u_3 potential, and it leads to an optical absorption dip at E_M. On the other hand, the mini-gap is more similar to an 'inverse gap' induced by a pure u_1 potential when $|u_1| > |u_3|$, which produces an optical absorption peak at E_M (Supplementary Section 4). The u_0 term does not affect the mini-gap at the m point, and only slightly modifies the optical absorption spectra. The observed absorption peak at E_M for charge neutral graphene (Fig. 3e) obviously cannot be described by the u_0 scalar potential, and it has a lineshape similar to that produced by the pseudospin-mixing u_1 term. It demonstrates unambiguously the spinor potential nature of the moiré superlattice potential, and shows that the pseudospin-mixing term u_1 is the dominant component. Quantitative comparison with the theory shows that the observed absorption spectrum can be described nicely using parameters obtained from a microscopic model (Supplementary Section 5) with $V_0 = 10$ meV and $(u_0, u_3, u_1) = (1/2, -\sqrt{3}/2, -1)$ (Fig. 3e). The positive value of V_0 arises from a stronger carbon–boron coupling than the carbon–nitrogen coupling, presumably owing to the significantly larger radius of the p orbital in boron than in nitrogen (Supplementary Section 5). The resulting electronic bandstructure from this set of parameters is shown in Fig. 3f. It exhibits a much stronger bandstructure change at the hole side,

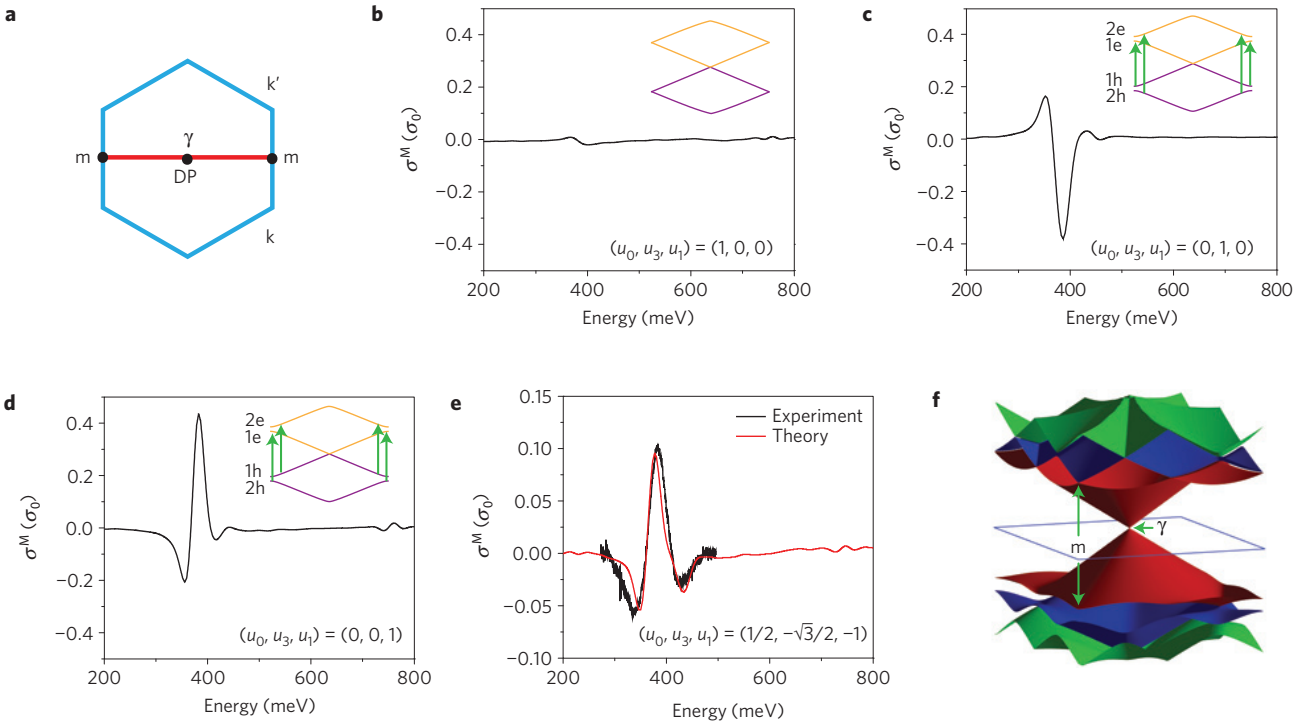

Figure 3 | Calculated optical conductivity changes under different spinor potentials. a, Mini-Brillouin zone of the moiré superlattice. The γ point corresponds to graphene's original Dirac point (DP). The mini-Brillouin zone boundary and edges are labelled with m and k/k′. Red line indicates the γ–m direction. **b**–**d**, Optical conductivity changes at the charge neutral point under u_0, u_3 and u_1 potentials, respectively, with $V_0 = 10$ meV. The insets show corresponding band structures along the γ–m direction and allowed optical transitions near the m point. **b**, The u_0 potential does not open a gap at the m point, and has small effect on optical conductivity. **c**, The u_3 potential opens a 'normal' gap, where optical transitions are restricted to symmetric 1e–1h and 2e–2h bands. This leads to a dip at E_M in optical conductivity. **d**, The u_1 potential opens an 'inverse' gap where only 1e–2h and 2e–1h transitions are allowed around the m point. Such transitions between parallel bands lead to an absorption peak at E_M due to a van Hove singularity in the joint density of states. **e**, Comparison of the experimental and theoretical optical conductivity change using the spinor potential from a microscopic model. **f**, Three-dimensional mini-band structure in the superlattice Brillouin zone with the parameters in **e**. The hole side is modulated much more strongly than the electron side.

consistent with the electron–hole asymmetry observed in electrical transport. This asymmetry is not pronounced in the optical data because optical transitions always involve both the electron and hole states.

Next, we examine the gate dependence of optical absorption spectra around E_M. We plot the peak height at E_M for different Fermi energies in Fig. 4, which shows a sharp decrease with increased electron concentration and goes almost to zero at $E_F \sim 140$ meV. This sensitive dependence on electron doping is very interesting because it cannot be explained by the single-particle Pauli blocking effect: the relevant Fermi energy is too low to block the electronic state transition at the m point (at $E_M/2 = 190$ meV, indicated by the dashed line). Therefore, the decreased absorption peak at E_M should originate from a change in the optical transition matrices, indicating that the spinor potential of the moiré superlattice is modified appreciably in doped graphene owing to electron–electron interactions. It is well known that dielectric screening from free carriers can reduce the scalar electrostatic potential, which can be calculated using the random phase approximation (RPA; ref. 31). If we assume that the effective spinor potential is screened like the scalar potential with wavevector $\mathbf{q}_M$, the RPA calculation predicts a rather weak decrease of the potential and the absorption peak with the carrier doping[31] (orange line in Fig. 4). Obviously the RPA approximation is not applicable to the spinor potential in graphene. Recent studies based on renormalization group theory show that the pseudospin-dependent potential is strongly renormalized by electron–electron interactions[29]. Presumably the spinor potential becomes weaker with electron doping owing to such renormalization effects, and the

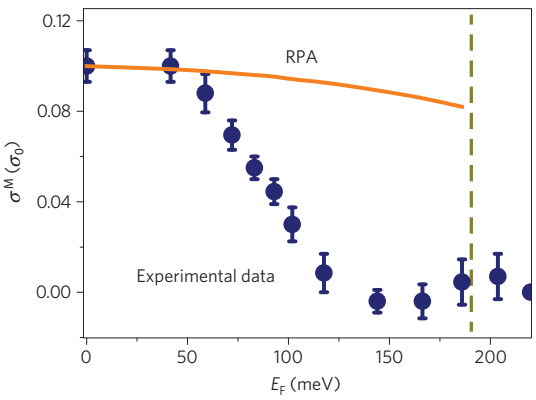

Figure 4 | Gate-dependent moiré spinor potential. The optical conductivity peak at E_M depends sensitively on the electron doping in graphene (symbols), and it diminishes before the optical transitions are affected by Pauli blocking (at the dashed vertical line). Error bars represent the uncertainty from fitting the spectra in Fig. 2b. (See Supplementary Information for more details.) This doping dependence suggests a strong renormalization of the moiré spinor potential by electron–electron interactions, which cannot be described by simple dielectric screening using the random phase approximation (RPA, orange line).

u_1 and u_3 parameters can have different renormalization behaviour. Further theoretical studies need to be carried out to quantitatively describe the experimental data.

Methods

Graphene samples were directly grown on hexagonal BN substrates without a catalyst following a van der Waals epitaxial mode. The growth was carried out in a remote plasma-enhanced chemical vapour deposition (R-PECVD) system at ~500 °C, with pure CH_4 as the carbon source. Hydrogen plasma etching was used after the growth to etch away the second layer and obtain a higher proportion of monolayer graphene. We used transmission electron microscope grids as shadow masks for metal electrode deposition. A long-working-distance optical microscope was employed to find BN flakes and align the shadow mask with the chosen BN flake. The deposited metal film has the form 2 nm/80 nm Ti/Au. Transmitted infrared spectra were measured using a Fourier transform infrared microscope (Thermo Nicolet Nexus 870 with a Continuum XL IR Microscope) with a synchrotron infrared light source. All the measurements were performed in vacuum at room temperature.

Received 7 May 2014; accepted 23 July 2014; published online 31 August 2014

References

1. Novoselov, K. S. *et al.* Electric field effect in atomically thin carbon films. *Science* **306,** 666–669 (2004).
2. Novoselov, K. S. *et al.* Two-dimensional gas of massless Dirac fermions in graphene. *Nature* **438,** 197–200 (2005).
3. Zhang, Y. B., Tan, Y. W., Stormer, H. L. & Kim, P. Experimental observation of the quantum Hall effect and Berry's phase in graphene. *Nature* **438,** 201–204 (2005).
4. Neto, A. H. C. *et al.* The electronic properties of graphene. *Rev. Mod. Phys.* **81,** 109–162 (2009).
5. Katsnelson, M. I., Novoselov, K. S. & Geim, A. K. Chiral tunnelling and the Klein paradox in graphene. *Nature Phys.* **2,** 620–625 (2006).
6. Geim, A. K. & Novoselov, K. S. The rise of graphene. *Nature Mater.* **6,** 183–191 (2007).
7. Wang, F. *et al.* Gate-variable optical transitions in graphene. *Science* **320,** 206–209 (2008).
8. Li, Z. Q. *et al.* Dirac charge dynamics in graphene by infrared spectroscopy. *Nature Phys.* **4,** 532–535 (2008).
9. Horng, J. *et al.* Drude conductivity of Dirac fermions in graphene. *Phys. Rev. B* **83,** 165113 (2011).
10. Min, H., Borghi, G., Polini, M. & MacDonald, A. H. Pseudospin magnetism in graphene. *Phys. Rev. B* **77,** 041407 (2008).
11. Jung, J., Zhang, F. & MacDonald, A. H. Lattice theory of pseudospin ferromagnetism in bilayer graphene: Competing interaction-induced quantum Hall states. *Phys. Rev. B* **83,** 115408 (2011).
12. San-Jose, P., Prada, E., McCann, E. & Schomerus, H. Pseudospin valve in bilayer graphene: Towards graphene-based pseudospintronics. *Phys. Rev. Lett.* **102,** 247204 (2009).
13. Park, C-H. *et al.* New generation of massless Dirac fermions in graphene under external periodic potentials. *Phys. Rev. Lett.* **101,** 126804 (2008).
14. Yankowitz, M. *et al.* Emergence of superlattice Dirac points in graphene on hexagonal boron nitride. *Nature Phys.* **8,** 382–386 (2012).
15. Ponomarenko, L. A. *et al.* Cloning of Dirac fermions in graphene superlattices. *Nature* **497,** 594–597 (2013).
16. Dean, C. R. *et al.* Hofstadter's butterfly and the fractal quantum Hall effect in moiré superlattices. *Nature* **497,** 598–602 (2013).
17. Hunt, B. *et al.* Massive Dirac fermions and Hofstadter butterfly in a van der Waals heterostructure. *Science* **340,** 1427–1430 (2013).
18. Yang, W. *et al.* Epitaxial growth of single-domain graphene on hexagonal boron nitride. *Nature Mater.* **12,** 792–797 (2013).
19. Zhang, Y. B. *et al.* Direct observation of a widely tunable bandgap in bilayer graphene. *Nature* **459,** 820–823 (2009).
20. McCann, E. Asymmetry gap in the electronic band structure of bilayer graphene. *Phys. Rev. B* **74,** 161403 (2006).
21. Ohta, T. *et al.* Controlling the electronic structure of bilayer graphene. *Science* **313,** 951–954 (2006).
22. Lui, C. H. *et al.* Observation of an electrically tunable band gap in trilayer graphene. *Nature Phys.* **7,** 944–947 (2011).
23. Son, Y. W., Cohen, M. M. & Louie, S. G. Half-metallic graphene nanoribbons. *Nature* **444,** 347–349 (2006).
24. Han, M. Y., Ozyilmaz, B., Zhang, Y. & Kim, P. Energy band gap engineering of graphene nanoribbons. *Phys. Rev. Lett.* **98,** 206805 (2007).
25. Avouris, P., Chen, Z. H. & Perebeinos, V. Carbon-based electronics. *Nature Nanotechnol.* **2,** 605–615 (2007).
26. Dean, C. R. *et al.* Boron nitride substrates for high-quality graphene electronics. *Nature Nanotechnol.* **5,** 722–726 (2010).
27. Wallbank, J. R. *et al.* Generic miniband structure of graphene on a hexagonal substrate. *Phys. Rev. B* **87,** 245408 (2013).
28. Kindermann, M., Uchoa, B. & Miller, D. L. Zero-energy modes and gate-tunable gap in graphene on hexagonal boron nitride. *Phys. Rev. B* **86,** 115415 (2012).
29. Song, J. C. W., Shytov, A. V. & Levitov, L. S. Electron interactions and gap opening in graphene superlattices. *Phys. Rev. Lett.* **111,** 266801 (2013).
30. Abergel, D. S. L. *et al.* Infrared absorption by graphene-hBN heterostructures. *New J. Phys.* **15,** 123009 (2013).
31. Hwang, E. H. & Das Sarma, S. Dielectric function, screening, and plasmons in two-dimensional graphene. *Phys. Rev. B* **75,** 205418 (2007).

Acknowledgements

We thank Z. Li and J. Song for helpful discussions. Device fabrication and optical measurements in this work were mainly supported by the Office of Naval Research (award N00014-13-1-0464). Electrical characterizations and theoretical analysis were supported by Office of Basic Energy Science, Department of Energy under contract Nos DE SC0003949 and DE AC02 05CH11231 (Materials Science Division). F.W. acknowledges support from a David and Lucile Packard fellowship. G.Z. acknowledges support from the National Basic Research Program of China (Grant No. 2013CB934500, 2012CB921302) and the National Natural Science Foundation of China (Grant No. 61325021, 91223204). The Advanced Light Source is supported by the Director, Office of Science, Office of Basic Energy Sciences, of the US Department of Energy under Contract No. DE-AC02-05CH11231.

Author contributions

F.W. and G.Z. conceived the research. W.Y. and X.L. grew the samples. Z.S., L.J. and D.F. fabricated the devices. Z.S., L.J., J.H. and H.A.B. carried out the optical measurements. C.J., F.W. and Z.S. developed the theory. Z.S., C.J., F.W. and G.Z. wrote the manuscript. All authors discussed the results and commented on the paper.

Additional information

Supplementary information is available in the online version of the paper. Reprints and permissions information is available online at www.nature.com/reprints. Correspondence and requests for materials should be addressed to F.W. or G.Z.

Competing financial interests

The authors declare no competing financial interests.